PHYSICAL REVIEW B **84**, 224116 (2011)

Polyamorphic transitions in Ce-based metallic glasses by synchrotron radiation

M. J. Duarte,[1,2] P. Bruna,[1] E. Pineda,[3] D. Crespo,[1] G. Garbarino,[4] R. Verbeni,[4] K. Zhao,[5]
W. H. Wang,[5] A. H. Romero,[2] and J. Serrano[6]
[1]*Departament de Fisica Aplicada, EPSC, Universitat Politècnica de Catalunya, C. Esteve Terradas 15, E-08860 Castelldefels, Spain*
[2]*Departamento de Materiales, CINVESTAV-Unidad Querétaro, Libramiento Norponiente 2000, 76230 Querétaro, Mexico*
[3]*Departament de Fisica i Enginyeria Nuclear, ESAB, Universitat Politècnica de Catalunya, C. Esteve Terradas 8, E-08860 Castelldefels, Spain*
[4]*European Synchrotron Radiation Facility, B.P. 220, 38043 Grenoble Cedex 9, France*
[5]*Institute of Physics, Chinese Academy of Sciences, 100080 Beijing, PR China*
[6]*ICREA - Departament de Fisica Aplicada, EPSC, Universitat Politècnica de Catalunya, C. Esteve Terradas 15, E-08860 Castelldefels, Spain*

(Received 23 June 2011; published 22 December 2011)

We report here on a polyamorphic-phase transition upon application of pressure on a Ce-based metallic glass, $Ce_{70}Al_{10}Ni_{10}Cu_{10}$, investigated by x-ray diffraction and inelastic x-ray scattering. This alloy is found to display a strong hysteresis in volume per atom upon application and subsequent release of pressure. The observed structural changes are correlated with changes observed by inelastic x-ray scattering in the elastic constants, acoustic mode frequencies, and sound speed. The results reported here point toward three different amorphous phases for this alloy existing in the 0–25 GPa pressure region: low- and high-density states and an intermediate mixed state that displays a hysteresis behavior. Finally, we discuss the impact of Ce concentration on the polyamorphic transition for a series of Ce-based metallic glass alloys and link it to the phase transformation between γ-Ce and α-Ce under pressure.

DOI: 10.1103/PhysRevB.84.224116 PACS number(s): 62.50.−p, 63.50.Lm, 64.70.kj, 81.30.Hd

I. INTRODUCTION

Phase transitions in single crystals have been known since the first applications of high-pressure research in the 1950s. The study of similar transitions in liquids and amorphous solids, however, has been undertaken much later due to the limited structural information available via x-ray and neutron-diffraction techniques. The evidence of a transition in amorphous ice when compressed at 77 K from a low-density state to a high-density amorphous ice at 0.6 GPa[1] changed the point of view concerning polyamorphism. Such transitions have been observed, for example, in liquid phosphorous[2] and sulfur,[3] by x-ray diffraction and neutron-diffraction techniques, respectively, for static signatures. Other examples of this phenomena include Si,[4–6] binary liquids such as Y_2O_3-Al_2O_3,[7,8] vitreous SiO_2,[9,10] and GeAsS chalcogenide glasses.[11]

More recently, metallic glasses (MGs) have attracted interest as a new class of amorphous materials due to their potential for structural applications.[12] The mixture of metallic binding with partial covalent bonds created by nonmetals, such as boron, carbon, silicon, and phosphorous, makes the study of polyamorphic transitions in MGs very appealing as a source of information about the role of the electronic structure on the transition.

Recently, polyamorphic transitions have been evidenced in nondirectional, densely-packed metallic glasses.[13] Using a combination of x-ray diffraction (XRD) experiments and theoretical calculations, a polyamorphic transition upon application of pressure was found in $Ce_{55}Al_{45}$ metallic glass in the 2–13.5 GPa range. XRD patterns showed hysteresis in the pressure dependence of the specific volume upon compression and decompression, with 14% density difference between the two amorphous states of the metallic glass at ambient pressure. Those results were compared with *ab-initio* calculations and discussed in terms of a pressure-driven change in the localization of Ce $4f$ electronic states, similar to the behavior observed in the γ–α phase transformation in crystalline cerium.[14,15] A similar case was later reported in $Ce_{75}Al_{25}$ metallic glass.[16]

The entanglement of structural polyamorphism with the specific electronic properties of cerium makes the case for recent research efforts devoted to the investigation of Ce-based MGs under pressure. Despite the extant evidence of structural changes and the role of Ce $4f$ electrons reported for these alloys, essential questions still remain unanswered, such as how these polyamorphism phenomena affect other material properties and to what extent the Ce content and its peculiar electronic behavior upon application of pressure drive the polyamorphic transition, namely volume collapse, transition pressure, and other parameters. Only recently, Zeng *et al.* reported a clear change in thermodynamic and electronic transport properties of $Ce_{75}Al_{25}$ as a result of the transition at 1.5 GPa.[17] Electronic delocalization may be anticipated to affect Ce-based MGs' mechanical properties. However, no direct observation has been achieved so far, partly due to the challenge of using traditional ultrasonic methods to reach the required high pressures. Inelastic x-ray scattering (IXS) provides unique access to this pressure range and, coupled with high-resolution XRD, allows one to shed light on the correlations between structural and mechanical changes.

We present here pressure-dependent studies of structural and mechanical properties of $Ce_{70}Al_{10}Ni_{10}Cu_{10}$ metallic glass. $Ce_{70}Al_{10}Ni_{10}Cu_{10}$ can be produced in a completely glassy state with a critical diameter of 3 mm,[18] and it is the first bulk metallic glass (BMG) reported with polyamorphism. XRD and IXS experiments using synchrotron radiation were carried out to account for static and dynamic signatures of the MG, respectively. We find three different amorphous regions in the 0–25 GPa pressure range and a different behavior upon application of pressure and decompression. For the chosen alloy, acoustic and elastic properties as functions of pressure up to 0.5 GPa, reported previously, show unusual behavior compared with other MGs.[19] Our IXS results agree with this behavior and allow one to understand the consequences of the polyamorphic transition in mechanical properties, i.e., longitudinal sound speed and elastic constant, up to 25 GPa, which covers the full transition between low- and high-density states. We also discuss the role of cerium content in the polyamorphic transition by a thorough analysis of the extant XRD data reported in the literature.

II. EXPERIMENTAL METHODS

The samples for both XRD and IXS experiments were cut from melt-spun ribbons stemming from a 4-mm diameter rod of $Ce_{70}Al_{10}Ni_{10}Cu_{10}$ produced by a mold cast. All experiments were conducted at room temperature on the same batch of ribbons, thus ensuring reliability and allowing for a direct comparison of structural and mechanical properties. The ribbons were loaded into diamond anvil cells (DAC) together with ruby pieces to calibrate and measure pressure using ruby fluorescence levels.[20,21]

XRD experiments were conducted in beamline ID27 at the European Synchrotron Radiation Facility (ESRF). Incident energy of 33 keV was focused on the sample by using the highly focalized micrometric-sized x-ray beam available at ID27 ($3 \times 2\ \mu m^2$). Small pieces of about 60 μm diameter and 30–50 μm thick were cut from the ribbons and inserted in the DAC for pressure application. Liquid helium was loaded into the DAC as a pressure-transmitting medium. XRD patterns were acquired in the 0–25 GPa pressure range upon both compression and decompression ramps in transmission mode through the diamonds. In the proximity of the sample, a diffraction pattern of the DAC was recorded solely at each pressure point. These spectra were used as background and subtracted from the sample signals after intensity normalization.

The IXS experiment was performed in beamline ID28 at the ESRF. The instrument was operated using the Si 999 Bragg reflection of the main monochromator, with an incident energy of 17.794 keV. This configuration yields a momentum transfer resolution of 0.27 nm^{-1} and an energy transfer resolution of 3 meV. IXS energy scans were performed in a range from -25 to 25 meV with an energy step of 0.5 meV for momentum transfers between 2 and 12 nm^{-1}. Spectra corresponding to eight different momentum transfers were recorded simultaneously using a multianalyzer setup. In order to optimize the IXS signal, 30–50 μm thick ribbons were selected and two samples of 170×150 and $95 \times 95\ \mu m^2$ were cut and mounted on the DACs. Liquid neon and helium were loaded in the DACs, together with the first and second samples, respectively, as pressure-transmitting mediums. The largest sample was used to obtain data up to 12.5 GPa, a pressure at which the DAC failed. The second sample was employed to obtain higher-pressure data and data upon decompression. Both data sets display a similar behavior at low pressure, which ensures reliability and the same hydrostatic conditions with both pressure-transmitting media.

III. RESULTS AND DISCUSSION

A. Structural properties

Figure 1 shows integrated XRD patterns obtained in beamline ID27 in the 0–25 GPa pressure range, upon both compression and decompression. The lower panels display intensity plots to highlight the spectral-weight redistribution in momentum transfer as a function of pressure. The samples remain amorphous in the whole pressure range, showing no signs of crystallization. A main peak is observed at 22.6 nm^{-1}, followed by broader features at 38.2 and 55.2 nm^{-1}. Upon compression, the main peak shifts to higher momentum transfer, displaying a distinct behavior at the lowest pressures. Below nearly 3 GPa, the peak shift occurs faster than at higher pressures, thus indicating the possible onset of the first amorphous-amorphous transformation. This shift is accompanied with a redistribution of the spectral weight corresponding to the second diffraction peak. It broadens and, at pressures larger than 2 GPa, a satellite structure appears at 50 nm^{-1}. This redistribution is more apparent in the lower panels. At higher pressure, the satellite also shifts to higher Q values with an increase in pressure, and both features decrease in relative intensity with respect to the main peak. Upon decompression, the same change in the intensity distribution is apparent at pressures lower than 4 GPa, and a sudden shift to lower momentum transfer of the main peak is observed below 2 GPa. The XRD patterns thus seem to reveal three distinct density regions, corresponding to the 0–2 GPa, 2–10 GPa, and higher pressure ranges, which points to the presence of phase transformations between amorphous structures for $Ce_{70}Al_{10}Ni_{10}Cu_{10}$. The approximate values where the transition occurs are more evident when the volume change is plotted, as seen in the inset of Fig. 2.

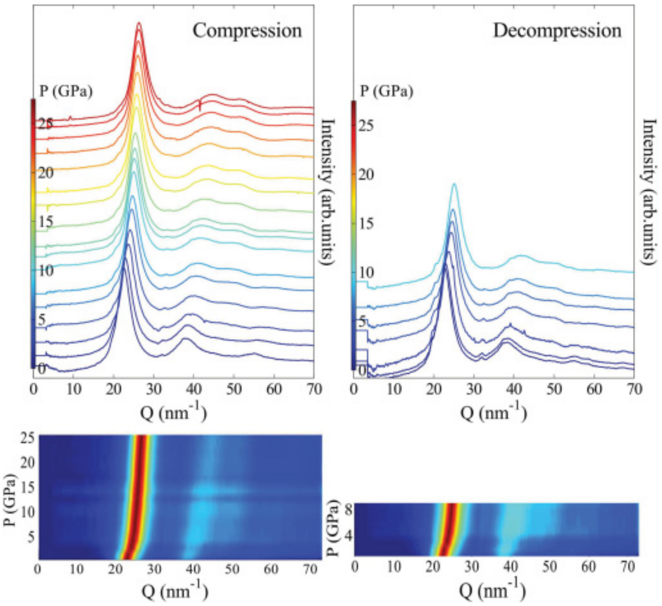

FIG. 1. (Color online) (XRD-integrated-intensity patterns of $Ce_{70}Al_{10}Ni_{10}Cu_{10}$ metallic glass obtained during compression and decompression. The lower panels display the intensity plot normalized to the intensity of the main diffraction peak, in order to highlight the spectral-weight redistribution.

Figure 2 displays the specific volume as a function of pressure for both compression and decompression processes. The volume ratio, V_P/V_0, was determined using the values of the momentum transfer at the main diffraction peak for each pressure point, observed in Fig. 1, where V_0 stands

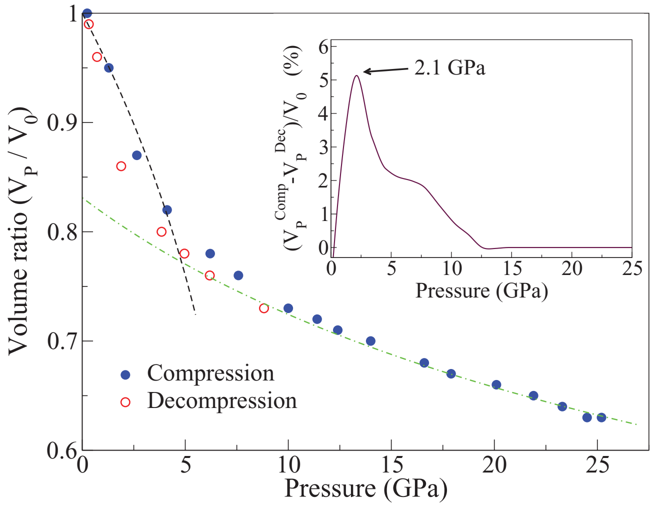

FIG. 2. (Color online) Relative specific volume versus pressure. Solid and open symbols correspond to data taken during compression and decompression, respectively. Dashed lines represent estimated EOS drawn to highlight the low- (black) and high- (green) density states observed at ambient and high pressure, respectively. The EOS corresponding to the low-density state, the upper black dashed line, was obtained from data up to 0.5 GPa, reported in Ref. 19. The inset shows the pressure dependence of the hysteresis by displaying the difference in volume ratio upon compression and decompression as a function of pressure.

for the specific volume estimated for the $Ce_{70}Al_{10}Ni_{10}Cu_{10}$ alloy at ambient pressure and temperature. Solid and open symbols correspond to data obtained during compression and decompression, respectively.

Upon application of pressure, two distinct regimes are clearly observed. The upper black dashed line at low pressure displays the equation of state (EOS) calculated from results up to 0.5 GPa, reported by Zhang *et al.*[19], and thus shows a reasonable agreement with our low-pressure data. The specific volume decreases faster between 0 to 4 GPa, in agreement with the shift in the main peak of the structure factor, shown in Fig. 1. At pressures larger than 10 GPa, the specific volume displays a pressure dependence that can be fitted to a general Murnaghan[22] type EOS (lower green dashed line). The latter fit was actually performed taking into account only pressure points above 15 GPa. Hence, these two regimes represent the low- and high-density states.

Between 4 and 10 GPa, the specific volume displays a nonlinear pressure dependence. Note the different convexity displayed by both EOSs, which points to either an anomalous pressure dependence of the specific volume or to the existence of a third region, where the convexity gradually changes. The latter might be the underlying reason for the hysteresis shown between the compression and decompression processes. In order to ascertain more clearly the pressure range of this mixed density region, in the inset of Fig. 2 we plot the change in specific volume between compression and decompression, as a function of pressure. To obtain this figure, spline interpolation curves of both up-load and down-load specific-volume data sets were subtracted. The data set for decompression was completed with those pressure points taken at pressures higher than 15 GPa, i.e., the high-pressure limit. This inset shows a peak change in volume ratio at nearly 2 GPa, with a maximum difference in volume ratio of nearly 5.5%, followed by a decrease in hysteresis up to 12 GPa. Despite the wiggles due to the reduced number of data points, an abrupt change in hysteresis is observed at 2 GPa, which makes us assign this pressure value to the onset of the intermediate density region.

Hence, these results suggest that $Ce_{70}Al_{10}Ni_{10}Cu_{10}$ metallic glass exhibits three different amorphous regions upon application of pressure. A low-density state is observed at ambient conditions, which becomes a higher-density state while pressure is increased. An intermediate region shows a gradual transition, which links both density states and displays hysteresis through compression and decompression stages. A volume collapse of ∼16% extrapolated at ambient pressure occurs between both density states. This hysteresis cycle and the large volume collapse are in agreement with previous works,[13,14,23] where the transition was assigned to be carried out by means of pressure-induced delocalizaton of Ce $4f$ electrons. Similar behavior was reported for $Ce_{75}Al_{25}$ MG, where an 8.6% volume collapse was observed at the same pressure as a transformation of Ce $4f$ electrons from a localized state at ambient pressure to an itinerant state at high pressure.[16] The origin of this polyamorphism can be attributed to a similar electronic transformation observed in crystalline cerium accompanying a phase transformation between γ–Ce and α–Ce, at 0.9 GPa.[14,15] We will return to this point in Sec. III.C.

B. Mechanical properties

Given the large electron-phonon coupling in Ce and the substantial amount of this element in the alloy,[24,25] changes in electronic-band structure should be followed by changes in phonon-dispersion relations and sound velocities.

High-pressure IXS experiments were performed to unveil the effect of the polyamorphic transition on the mechanical properties of Ce-based alloys at a microscopic level. In order to cover the full pressure range up to a complete transition, IXS spectra were acquired from 0 to 22 GPa, as pressure increased, and at 10 GPa, as pressure decreased.

Figure 3(a) displays representative IXS spectra for the eight values of the momentum transfer obtained simultaneously at 0.4 GPa. The spectra consist of a central elastic peak at zero-energy transfer followed by additional peaks at positive and negative energies that correspond to longitudinal acoustic excitations of $Ce_{70}Al_{10}Ni_{10}Cu_{10}$ metallic glass. The elastic peak has been truncated in order to enhance the features corresponding to acoustic waves.

The IXS spectra are proportional to the dynamic structure factor, $S(Q,w)$. They can be fitted by using, as a model function, a damped harmonic oscillator for each excitation and a delta function for the elastic line. Both are convoluted with the experimental resolution function[26]

$$\frac{S(Q,\omega)}{S(Q)} = A(Q)\delta(\omega) + \frac{1-A(Q)}{\pi} \times \frac{\Omega^2(Q)\Gamma(Q)}{[\omega^2-\Omega^2(Q)]^2+\omega^2\Gamma^2(Q)}, \tag{1}$$

where, at a given momentum transfer Q, $S(Q)$ is the static-structure factor measured using standard x-ray diffraction;

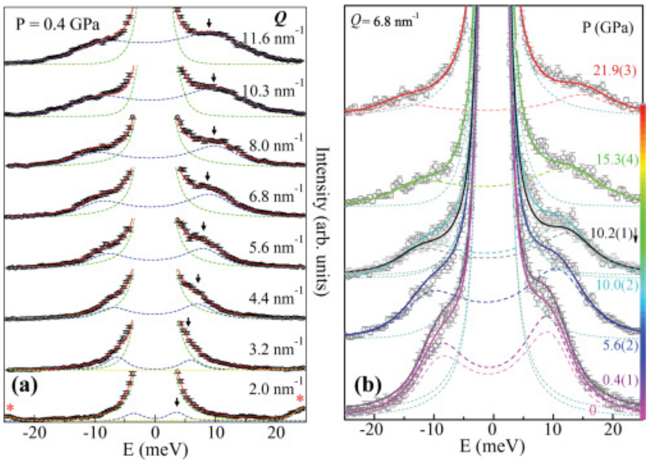

FIG. 3. (Color online) Selected IXS spectra of the $Ce_{70}Al_{10}Ni_{10}Cu_{10}$ metallic glass for (a) pressure of 0.4 GPa and Q between 2 and 12 nm^{-1}, and (b) pressures up to 22 GPa and $Q = 6.8$ nm^{-1}. Open circles correspond to experimental data and solid lines to the best fit obtained using Eq. (1). The individual components of the excitation (blue) and the elastic line (green) are displayed with dashed lines.

$A(Q)$ is the intensity of the elastic scattering relative to the spectrum total intensity; $\Omega(Q)$ is the characteristic frequency of the acoustic mode and corresponds to the maximum of the longitudinal current spectra $C_L(Q,\omega) = (\omega/Q)^2 S(Q,\omega)$; and $\Gamma(Q)$, denoted as phonon damping, is a parameter related to the sound attenuation and the full-width-at-half-maximum (FWHM) of the excitation signal.[26] Dashed lines represent the elastic (green) and inelastic (blue) contributions derived from the model after convolution to the experimental instrumental function, which is analyzer-dependent. At the lowest momentum transfer, a transverse acoustic phonon of diamond from the anvil cell appears and is marked with a red asterisk. Due to the higher sound speed of this mode, 11 km/s, it goes out of the region of interest with increases in momentum transfer.

The broadening of acoustic excitations as momentum transfer increases indicates an increase in the sound attenuation, up to a point where the broadening becomes so large that it is no longer valid for the term of propagating excitations to refer to the modes.[27]

The energy of these acoustic-like excitations has a typical behavior of acoustic modes. First, it increases as the momentum transfer increases at low Q values and then starts to decrease when the highest Q values are reached, as displayed by the arrows in Fig. 3(a). Second, the excitation intensity increases as well with Q, due to both the increase of the broadening and the energy.

Figure 3(b) shows selected IXS spectra corresponding to a momentum transfer of 6.8 nm^{-1} upon compression up to 22 GPa, and at 10.2 GPa in decompression. With increasing pressure, a blue shift of the excitation energy occurs. This corresponds to a stiffening of the amorphous medium upon application of pressure, similar to that observed in single crystals. The energy of the excitations increases as pressure increases, and it follows an almost linear relation. On the other hand, the intensity decreases when higher pressure is applied, which might be attributed to changes in the pressure-transmitting medium.

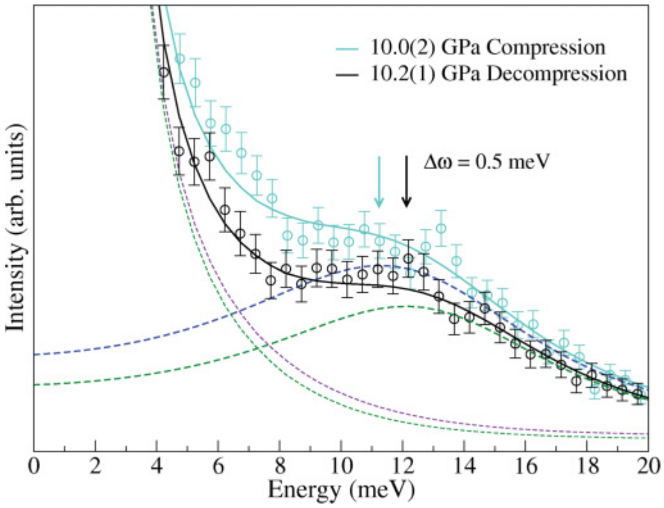

FIG. 4. (Color online) Example of different behavior of the IXS-intensity-band shift during compression and decompression at around 10 GPa and 6.8 nm^{-1}.

A close-up of the IXS curves during compression and decompression at Q = 6.8 nm^{-1} is presented in Fig. 4. The lower intensity of excitation during decompression suggests an hysteresis effect on the mechanical properties of the $Ce_{70}Al_{10}Ni_{10}Cu_{10}$ metallic glass going upward and downward during the structural polyamorphic transition. This hysteresis is further emphasized by the 0.5 meV energy increase observed at the excitation energy from compression to decompression. At lower momentum transfers, the IXS spectra, taken during the pressure increase and decrease processes, almost retrace each other and the energy shift becomes negligible. At 11.6 nm^{-1}, however, the energy shift becomes more than double, thus providing evidence that the hysteresis in structural properties also creates an hysteresis in mechanical properties.

Similar to the results for single crystals at a given pressure, the dependence of the acoustic-excitation energy on the momentum transfer can be plotted in a diagram, and it follows a dispersing curve, the so-called longitudinal acoustic dispersion relation for the amorphous material. The dispersion relation has an almost linear dependence on Q when Q tends to zero, and its slope at this limit corresponds to the macroscopic longitudinal sound velocity.[28] Figure 5(a) displays such dispersion curves obtained at different pressures from the excitation energies shown in the previous figures. The dispersion curves behave like a typical sinusoidal function that peaks at momentum transfers between 10 and 12 nm^{-1}, depending on the applied pressure. This maximum turns out to be at the same momentum transfer $Q_{\max}$ as half that of the main peak of the static structure factor determined with XRD, which suggests that the amorphous material presents a pseudo-Brillouin zone of characteristic length equal to $2Q_{\max}$. Note the different value of $Q_{\max}$ observed at 10 GPa for the pressure-increase and the pressure-decrease processes. This again reflects the structural hysteresis observed in the polyamorphic transition. An anomalous behavior is observed at low pressures, where a softening of the longitudinal acoustic

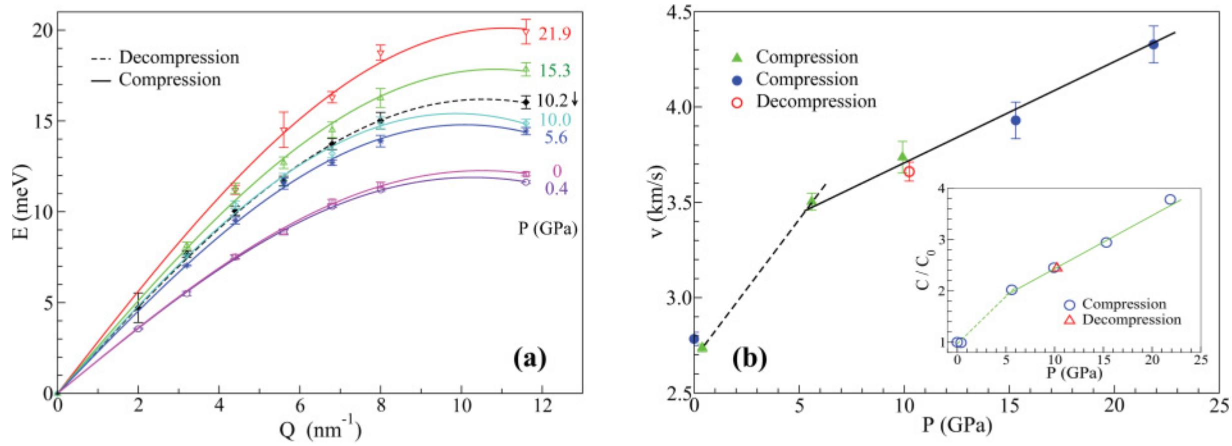

FIG. 5. (Color online) (a) The dispersion relation of the inelastic excitations obtained from a damped harmonic oscillator model. (b) Sound velocity dependence on hydrostatic pressure. The inset displays the change with pressure of the relative longitudinal elastic constant.

mode with an increase of pressure between 0 and 0.4 GPa is clearly shown in Fig. 5(a).

The longitudinal sound velocity was obtained by extrapolating a sinusoidal fit of the dispersion relations to zero-momentum transfer and by taking the slope at this limit for each pressure. Calculated velocities are displayed in Fig. 5(b). By following this procedure, a longitudinal sound speed of 2.78 km/s is obtained at ambient pressure. Different symbols are used to represent data stemming from different samples taken during compression and decompression. A pressure-induced decrease in sound velocity of ∼1.4% is observed at low pressure. This decrease correlates with the softening of the mode observed in Fig. 5(a).

It is worthwhile to notice that a negative slope in the change of acoustic velocities as a function of pressure is characteristic of glasses with covalent bonds. The followed behavior is in agreement with the negative change in the acoustic longitudinal velocity shown by Zhang *et al.*,[19] where measurements up to 0.5 GPa were reported. At higher pressures, a sudden increase in sound velocity is observed between 0.4 and 5 GPa, followed by a linear rise at a smaller rate up to the highest applied pressure of 22 GPa. This last behavior is expected from other bulk MGs.[29] Results presented in Fig. 5 show the presence of a transition from a more covalent phase at low pressure to a metallic one when pressure is increased. Unfortunately, more data points are required to reveal at which pressure the change in slope occurs and whether this change is abrupt or smooth. However, 5 GPa is a higher-limit-pressure value for the transition, which agrees well with the changes in the static-structure factor, obtained from XRD and shown in Figs. 1 and 2. The fact that the pressure dependence of the sound velocity changes twice over the slope between 0 and 25 GPa point to at least three phases of distinct mechanical behaviors displayed by amorphous $Ce_{70}Al_{10}Ni_{10}Cu_{10}$, in line with the three pressure ranges of different density defined solely from analysis of the XRD data. Upon a decrease of pressure, the sound velocity becomes slightly smaller than that obtained in the upload process, thus showing again the nonreversible character of the polyamorphic transition.

The sound velocity, v, is related to the longitudinal elastic constant of $Ce_{70}Al_{10}Ni_{10}Cu_{10}$, given as C, by the following expression: $C = v^2\rho$, where ρ is the mass density, i.e., inversely proportional to the specific volume. The inset of Fig. 5(b) displays the combination of both the static and dynamic effects of the polyamorphic transition by showing the pressure dependence of C relative to its value at ambient pressure, C_0. Two changes are again observed. A softening of C from 0 to 0.4 GPa is followed by a sudden stiffening of the elastic constant up to 5 GPa, followed by a linear behavior up to the applied highest pressure of 22 GPa. The three regions displayed by the pressure dependence of C further strengthen the three density domains described in Sec. III A. Since the sound velocity decreases from compression to decompression and the specific volume also decreases from one to the other, a partial cancellation of both effects is to be expected for the elastic constant. In agreement with this and within the experimental resolution, no hysteresis can be assigned to the elastic constant, although more IXS data upon decompression are required to make a firm statement. The extrapolation of the elastic constant of the high-density state to ambient pressure reveals a stiffening of 20% with respect to the low-density state, at 0 GPa, as a consequence of the polyamorphic transition.

The IXS data, therefore, confirm the existence of three different mechanical behaviors of amorphous $Ce_{70}Al_{10}Ni_{10}Cu_{10}$ in the 0 to 22 GPa pressure range. The negative slope of both longitudinal sound velocity and elastic constant at low pressure corresponds with a softening of the mode energies typical of glasses with covalent bonds. The intermediate pressure range thus corresponds to a change from covalent-like to metallic-like bonding behavior in glasses under pressure, which then stabilizes at higher pressures. More IXS pressure points are required to establish the transition between these three regions.

C. Discussion

The combination of both XRD and IXS point to a gradual nonreversible transition between a low-density and a high-density state. The origins of this transition can be traced back to crystalline cerium, which exhibits a polymorphic transition stemming from the $4f$ electrons' strong correlation.[14,15]

Experimentally, the fcc α phase of Ce transforms into a fcc γ phase when temperature is increased, and the transformation is linked to a large change in the volume. When pressure is applied at room temperature, the isostructural γ–α phase transition is observed at around 0.9 GPa accompanied with a decrease in volume of 15%. This structural behavior has been linked to the electronic behavior of the $4f$ electrons of Ce, and pressure-induced delocalization was observed. This delocalization has been recently reported to induce strong changes in both phonon dispersions and a strong electron-phonon coupling.[30]

Unlike crystalline Ce, in which the transition occurs sharply, polyamorphic transitions in Ce-based metallic glasses are smooth and continuous over a pressure range and present a hysteresis cycle by decreasing pressure. It is therefore expected that changing the Ce concentration will allow for a detailed study of the interplay between electronic and lattice roles in the polyamorphic transformation.

Figure 6 summarizes the estimated volume reduction and the pressure range at which the transition takes place in different Ce-based alloys. It also includes the results obtained in this research. The value of the starting pressure of the transition for the lowest Ce concentration MG is not reported in the literature. A larger pressure range is observed when Ce concentration decreases, with a saturation for the final pressure at 50% Ce atom concentration. This can be explained by considering the local environments in each alloy. Crystalline Ce owns a unique and identical structure throughout the material, and the transformation occurs at the same time for all atoms. Adding foreign atoms increases the disorder in the alloy and modifies the local environment of Ce. Therefore, a change in coordination as well as in electronic properties is also observed. In Ce-based metallic glasses, the smallest pressure range and volume collapse for the transformation occurs for $Ce_{75}Al_{25}$ metallic glass,[16] which shares the stoichiometric concentration of the $AlCe_3$ intermetallic phase. When a small concentration of aluminum is substituted by a more covalent atom, such as silicon, as in $Ce_{75}Al_{23}Si_2$ metallic glass,[31] the transition pressure is modified, and displays a transition-pressure range twice as large as that for the parent compound. With the incorporation of more foreign atoms and the consequent reduction of the Ce concentration in $Ce_{70}Al_{10}Ni_{10}Cu_{10}$, $Ce_{55}Al_{45}$,[13] and $Ce_{32}La_{32}Al_{16}Ni_5Cu_5$,[32] the alloys transform at different rates and the pressure range of the transformation and the volume reduction increase as the Ce-Ce coordination decreases. Below a certain critical Ce atomic concentration, the $4f$ electron correlation effects are expected to decrease dramatically, and therefore further dilution of cerium does not alter the final pressure of the transformation. Finally, note that for all reported values the transformation starts around 2 GPa. It is independent of the Ce concentration and occurs at pressures relatively close to that of the polymorphic transformation of crystalline cerium.

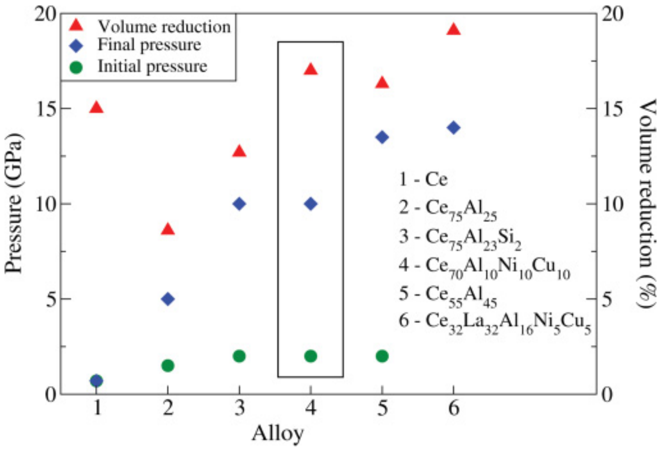

FIG. 6. (Color online) Pressure range of the polyamorphic transition and volume reduction observed in different Ce-based metallic glasses. Data were taken from Refs. 13, 16, 31, and 32 except for the $Ce_{70}Al_{10}Ni_{10}Cu_{10}$ metallic glass.

We expect that this paper will stimulate further IXS investigations on Ce-based MGs under pressure to uncouple electronic and lattice degrees of freedom and achieve a better comprehension of polyamorphic transformations in these alloys. A step further in the investigation of polyamorphic transitions in Ce-based alloys will require the ability to ascertain specific changes in the electronic structure and bonding driven by Ce $4f$ localization and accessed by inelastic x-ray scattering in the eV energy range. This has not yet been undertaken. Further information can be obtained by x-ray absorption experiments under pressure, which would uncover the local atomic rearrangements that take place at the electronic delocalization and the polyamorphic macroscopic transition.

IV. CONCLUSIONS

We have reported a thorough investigation of the behavior of structural and mechanical properties of $Ce_{70}Al_{10}Ni_{10}Cu_{10}$ by x-ray diffraction and inelastic x-ray scattering upon application of pressure up to 25 GPa. Low- and high-density amorphous phases were found at different pressure ranges, with an intermediate density region, which could be a mixture of both phases between 2 and 10 GPa. Decompression from the high-density phase results in a reversible change to the ambient-pressure phase, though hysteresis is observed in the static structure factor for the intermediate-density region. The XRD results correlate well with changes in pressure in the longitudinal acoustic sound speed and the associated elastic constant, as revealed by IXS experiments. The hysteresis in structural changes affects the acoustic sound speed and becomes more apparent in the comparison of acoustic-mode energies at high momentum transfers. Both structural and dynamical hysteresis effects seem to cancel each other in the estimate of the longitudinal elastic constant.

The observed polyamorphic transition in $Ce_{70}Al_{10}Ni_{10}Cu_{10}$ upon application of pressure is attributed to a change in Ce $4f$ electrons from a localized electronic structure to an itinerant one, similar to the results reported for other Ce-based MGs and for crystalline Ce. The analysis of reported data on similar polyamorphic transitions for other Ce-based amorphous alloys reveals a broadening of the intermediate-density region with increasing atomic alloying and reducing Ce content related to higher diversity of local environments in the more complex Ce-based metallic glasses. This broadening seems to saturate upon decrease of Ce concentrations below 55%. The lower limit for the polyamorphic transformation remains nearly unchanged, at 2 GPa, i.e., double the γ–α transition in crystalline cerium, up to a concentration of 55% atomic cerium. Further IXS experiments on intermediate Ce-content amorphous alloys are required to fully uncouple the role of Ce $4f$ electrons from lattice degrees of freedom in the polyamorphic transformation.

ACKNOWLEDGMENTS

We acknowledge the European Synchrotron Radiation Facility for provision of synchrotron radiation facilities under proposals CGR-16-01-726 and HD-349, and we would like to thank A. Labrador for assistance in using beamline BM16. EP, DC and JS acknowledge financial support from CICYT Grant No. MAT2010-14907 and Generalitat de Catalunya Grant No. 2009SGR1225. PB acknowledges financial support from Generalitat de Catalunya Grant No. 2009SGR1251. MJD and AHR acknowledge support from Conacyt, México, through projects PPPROALMEX-DAAD-Conacyt and 152153. WHW acknowledges financial support from NSF of China (Grants No. 50921091 and No. 50731008) and MOST973 of China (Grants No. 2007CB613904 and No. 2010CB731603).

---

[1] O. Mishima, L. D. Calvert, and E. Whalley, Nature (London) **314**, 76 (1985).

[2] Y. Katayama, T. Mizutani, W. Utsumi, O. Shimomura, M. Yamakata, and K. Funakoshi, Nature (London) **403**, 170 (2000).

[3] R. Winter, C. Szornel, W. C. Pilgrim, W. S. Howells, P. A. Egelstaff, and T. Bodensteiner, J. Phys.: Condens. Matter **2**, 8427 (1990).

[4] T. Morishita, Phys. Rev. Lett. **93**, 055503 (2004).

[5] S. K. Deb, M. Wilding, M. Somayazulu, and P. F. McMillan, Nature (London) **414**, 528 (2001).

[6] S. Sastry and C. A. Angell, Nat. Mater. **2**, 739 (2003).

[7] M. C. Wilding and P. F. McMillan, J. Non-Cryst. Solids **293**, 357 (2001).

[8] P. F. McMillan and M. C. Wilding, J. Non-Cryst. Solids **354**, 1015 (2008).

[9] C. Meade, R. J. Hemley, and H. K. Mao, Phys. Rev. Lett. **69**, 1387 (1992).

[10] L. Huang, L. Duffrene, and J. Kieffer, J. Non-Cryst. Solids **349**, 1 (2004).

[11] S. Sen, S. Gaudio, B. G. Aitken, and C. E. Lesher, Phys. Rev. Lett. **97**, 025504 (2006).

[12] M. F. Ashby and A. L. Greer, Scr. Mater. **54**, 321 (2006).

[13] H. W. Sheng, H. Z. Liu, Y. Q. Cheng, J. Wen, P. L. Lee, W. K. Luo, S. D. Shastri, and E. Ma, Nat. Mater. **6**, 192 (2007).

[14] P. Soderlind, Adv. Phys. **47**, 959 (1998).

[15] A. B. Shick, W. E. Pickett, and A. I. Liechtenstein, J. Electron Spectrosc. Relat. Phenom. **114**, 753 (2001).

[16] Q. S. Zeng, Y. Ding, W. L. Mao, W. Yang, S. V. Sinogeikin, J. Shu, H. K. Mao, and J. Z. Jiang, Phys. Rev. Lett. **104**, 105702 (2010).

[17] Q. S. Zeng, V. V. Struzhkin, Y. Z. Fang, C. X. Gao, H. B. Luo, X. D. Wang, C. Lathe, W. L. Mao, F. M. Wu, H.-K. Mao, and J. Z. Jiang, Phys. Rev. B **82**, 054111 (2010).

[18] B. Zhang, R. J. Wang, D. Q. Zhao, M. X. Pan, and W. H. Wang, Phys. Rev. B **70**, 224208 (2004).

[19] B. Zhang, R. J. Wang, and W. H. Wang, Phys. Rev. B **72**, 104205 (2005).

[20] H. K. Mao and P. M. Bell, Science **191**, 851 (1976).

[21] Z. Liu, Q. Cui, and G. Zou, Phys. Lett. A **143**, 79 (1990).

[22] F. D. Murnaghan, Proc. Natl. Acad. Sci. USA. **30**, 244 (1944).

[23] A. Svane, W. M. Temmerman, Z. Szotek, J. Lægsgaard, and H. Winter, Int. J. Quantum Chem. **77**, 799 (2000).

[24] W. E. Pickett, Physica B **111**, 1 (1981).

[25] G. Rout, M. S. Ojha, and S. N. Behera, Physica B **367**, 101 (2005).

[26] T. Scopigno, J. B. Suck, R. Angelini, F. Albergamo, and G. Ruocco, Phys. Rev. Lett. **96**, 135501 (2006).

[27] B. Rufflé, G. Guimbretière, E. Courtens, R. Vacher, and G. Monaco, Phys. Rev. Lett. **96**, 045502 (2006).

[28] G. Monaco, C. R. Phys. **9**, 608 (2008).

[29] W. H. Wang, F. Y. Li, M. X. Pan, D. Q. Zhao, and R. J. Wang, Acta Mater. **52**, 715 (2004).

[30] M. Krisch, D. L. Farber, R. Xu, D. Antonangeli, C. M. Aracne, A. Beraud, T.-C. Chiang, J. Zarestky, D. Y. Kim, E. I. Isaev, R. Ahuja, and B. Johansson, Proc. Natl. Acad. Sci. USA. **108**, 9342 (2011).

[31] Q. S. Zeng, Y. Z. Fang, H. B. Lou, Y. Gong, X. D. Wang, K. Yang, A. G. Li, S. Yan, C. Lathe, F. M. Wu, X. H. Yu, and J. Z. Jiang, J. Phys. Condens. Matter **22**, 375404 (2010).

[32] Q. S. Zeng, Y. C. Li, C. M. Feng, P. Liermann, M. Somayazulu, G. Y. Shen, H. K. Mao, R. Yang, J. Liu, T. D. Hu, and J. Z. Jiang, Proc. Natl. Acad. Sci. USA. **104**, 13565 (2007).